

# Observed impacts of COVID-19 on urban CO<sub>2</sub> emissions

Alexander J. Turner<sup>1,2,3\*</sup>, Jinsol Kim<sup>1</sup>, Helen Fitzmaurice<sup>1</sup>, Catherine Newman<sup>2</sup>, Kevin Worthington<sup>2</sup>, Katherine Chan<sup>2</sup>, Paul J. Wooldridge<sup>2</sup>, Philipp Köhler<sup>4</sup>, Christian Frankenberg<sup>3,4</sup>, and Ronald C. Cohen<sup>1,2</sup>

<sup>1</sup>Department of Earth and Planetary Sciences, University of California, Berkeley, CA, 94720, USA

<sup>2</sup>College of Chemistry, University of California, Berkeley, CA, 94720, USA

<sup>3</sup>Jet Propulsion Laboratory, California Institute of Technology, Pasadena, CA, 91109, USA

<sup>4</sup>Division of Geological and Planetary Sciences, California Institute of Technology,

## Key Points:

- Observe a 30% decrease in urban CO<sub>2</sub> emissions from the San Francisco Bay Area in response to COVID-19 mobility restrictions
- Changes are primarily driven by a decrease in CO<sub>2</sub> emissions from traffic (-48%)
- Large change to the weekly and diurnal cycle of emissions with reductions in morning rush-hour emissions

---

\*now at: Department of Atmospheric Sciences, University of Washington, Seattle, WA, 98195, USA

Corresponding author: Ronald C. Cohen, [rccohen@berkeley.edu](mailto:rccohen@berkeley.edu)

Corresponding author: Alexander J. Turner, [turneraj@uw.edu](mailto:turneraj@uw.edu)

This article has been accepted for publication and undergone full peer review but has not been through the copyediting, typesetting, pagination and proofreading process which may lead to differences between this version and the Version of Record. Please cite this article as doi: [10.1029/2020GL090037](https://doi.org/10.1029/2020GL090037)

**Abstract**

Governments restricted mobility and effectively shuttered much of the global economy in response to the COVID-19 pandemic. Six San Francisco Bay Area counties were the first region in the United States to issue a “shelter-in-place” order asking non-essential workers to stay home. Here we use CO<sub>2</sub> observations from 35 Berkeley Environment, Air-quality and CO<sub>2</sub> Network (BEACO<sub>2</sub>N) nodes and an atmospheric transport model to quantify changes in urban CO<sub>2</sub> emissions due to the order. We infer hourly emissions at 900-m spatial resolution for 6 weeks before and 6 weeks during the order. We observe a 30% decrease in anthropogenic CO<sub>2</sub> emissions during the order and show this decrease is primarily due to changes in traffic (-48%) with pronounced changes to daily and weekly cycles; non-traffic emissions show small changes (-8%). These findings provide a glimpse into a future with reduced CO<sub>2</sub> emissions through electrification of vehicles.

**Plain Language Summary**

This work uses atmospheric observations to quantify the changes in urban CO<sub>2</sub> emissions from different sectors in response to COVID-19 mobility regulations.

**1 Introduction**

Carbon dioxide (CO<sub>2</sub>) is an atmospheric trace gas responsible for most of the growth in anthropogenic radiative forcing (IPCC, 2013). Mitigating long-term climate change necessitates drastic reductions to our CO<sub>2</sub> emissions. Specifically, limiting global mean warming to 1.5°C requires reaching net-zero anthropogenic CO<sub>2</sub> emissions by 2050 (IPCC, 2018). Over 70% of these anthropogenic CO<sub>2</sub> emissions in the United States are attributable to urban areas (EIA, 2015; Hutyra et al., 2014); as such, it is important to be able to accurately quantify the emissions from these regions to support regulatory policies aimed at CO<sub>2</sub> reduction and provide citizens with metrics indicating their effectiveness.

The abrupt shuttering of the global economy in response to the COVID-19 global pandemic presents an opportunity to evaluate methods for quantifying urban CO<sub>2</sub> emissions, to assess our ability to attribute emissions to specific source sectors, and to describe the changes in emissions from different sectors. Understanding the changes that occurred during the COVID-19 period will allow us to identify: 1) the magnitude and subset of CO<sub>2</sub> emissions that respond to changes in our travel to/from workplaces on short time scales and 2) the sectors whose emissions persist irrespective of changes in urban travel patterns. Recent research used changes in activity data to predict the impact of COVID-19 on global CO<sub>2</sub> emissions and inferred a -17% (-11% to -25%) change in global daily CO<sub>2</sub> emissions (Le Quéré et al., 2020). This prediction has yet to be confirmed with measurements of atmospheric CO<sub>2</sub>.

The focus of this study is the San Francisco Bay Area in Northern California as it was the first region in the United States to enact regulations on mobility through a “shelter-in-place” (SIP) order on March 16, 2020 (Contra Costa County Health Officer, 2020). We use a dense network of CO<sub>2</sub> observations across the north eastern region of the San Francisco Bay Area to quantify the impacts of the SIP order on urban CO<sub>2</sub> emissions. Figure 1A shows the spatial coverage of our ground-based network of *in situ* sensors: the Berkeley Environmental Air-quality & CO<sub>2</sub> Network (BEACO<sub>2</sub>N; Shusterman et al., 2016; Turner et al., 2016; Kim et al., 2018; Shusterman et al., 2018). Shusterman et al. (2016) and Supplemental Section S1 give additional details on the network. We examine data from the study period between February 2, 2020 and May 2, 2020, during which 35 sensors were operational.

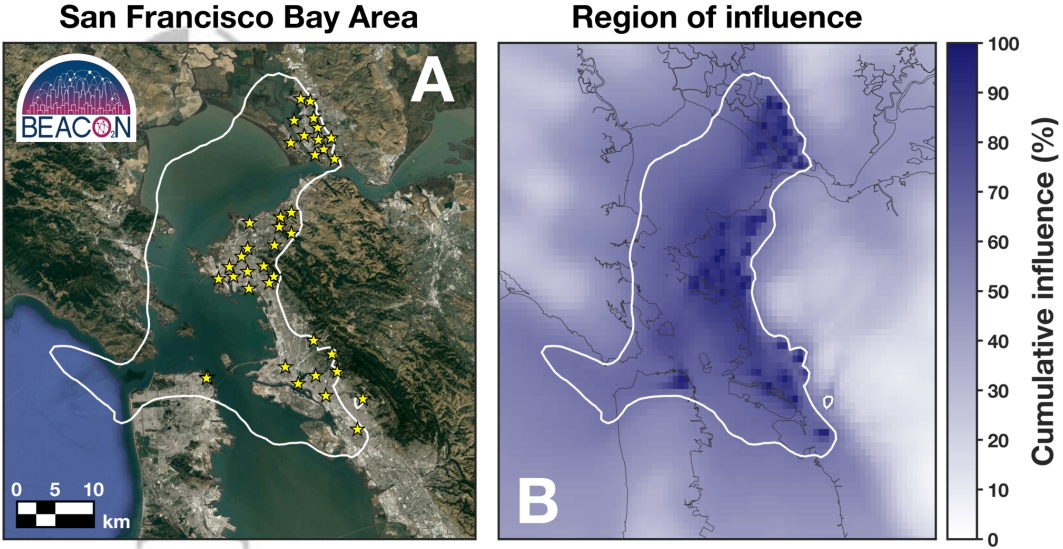


**Figure 1.** Observational network in the San Francisco Bay Area. Panel A shows the location of instruments in the Berkeley Environmental Air-quality & CO<sub>2</sub> Network (BEACO<sub>2</sub>N; yellow stars). Panel B shows the cumulative influence to the network derived from STILT footprints for observations in March 2020. White contour in both panels indicates the region that contains the largest 40% of the total network influence (referred to as the “BEACO<sub>2</sub>N Domain”).

## 2 Atmospheric Inversion Framework

Figure 2 shows a comparison of the network-wide median CO<sub>2</sub> concentrations for each day-of-week for six weeks before and during the SIP order. We observe a 5–50 ppm decrease in mid-week CO<sub>2</sub> concentrations with the most pronounced changes on Monday through Thursday during the morning rush-hour (~07:00 local time). Weekend concentrations show small differences in the median between the two time periods, although the variability is somewhat larger before the SIP. These observations suggest: 1) large reductions in CO<sub>2</sub> emissions occurred due to the SIP order and 2) marked changes to both the daily and weekly cycle of emissions due to shifts in human activity. Quantifying and attributing changes in CO<sub>2</sub> concentrations to emissions requires accounting for the coupling of meteorology and emissions.

We use the Stochastic Time-Inverted Lagrangian Transport model (STILT; Lin et al., 2003; Fasoli et al., 2018) with meteorology from the NOAA High Resolution Rapid Refresh (HRRR; Kenyon et al., 2016) to both estimate the sensitivity of each measurement to upwind emission sources and estimate the concentration upwind of our domain. Supplemental Section S2 provides details on the transport modeling. Each measurement ( $y_i$ ) has a unique background concentration ( $b_i$ ; see Supplemental Section S3) and footprint ( $\mathbf{h}_i$ ). The footprint represents the spatio-temporal region that an atmospheric measurement is sensitive to (i.e., the region that could influence a measurement); see Lin et al. (2003), Fasoli et al. (2018), and Turner et al. (2016, 2018) for additional details on constructing the footprints.

The measurements are related to the surface CO<sub>2</sub> emissions ( $\mathbf{x}$ ) as:  $y_i = \mathbf{h}_i \mathbf{x} + b_i$  and we use Bayesian inference to obtain hourly CO<sub>2</sub> emissions at 900-m spatial resolution from the atmospheric measurements. Prior fluxes are adapted from previous work (Turner et al., 2016; McDonald et al., 2014) but now use a biosphere derived from measurements of solar-induced chlorophyll fluorescence (SIF; Turner et al., 2020, *under review*). Additionally, we manually inspected the 20 largest point sources to ensure they were spa-

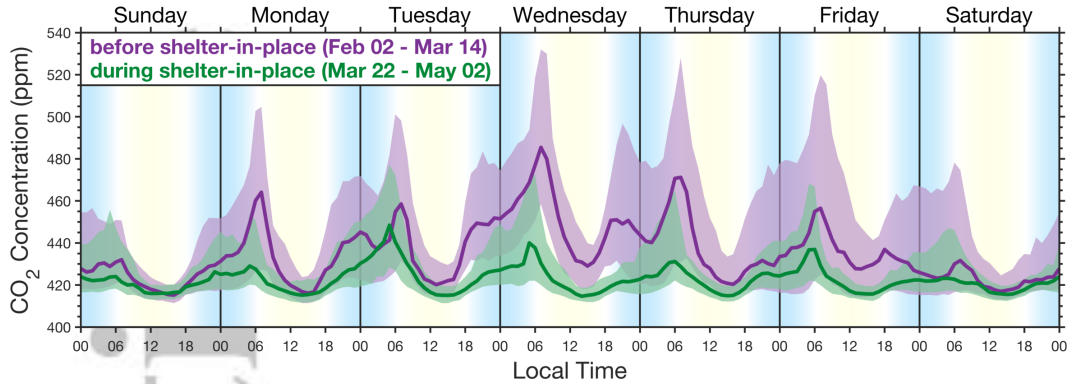


**Figure 2. Weekly CO<sub>2</sub> concentrations before and during shelter-in-place order.**

Solid lines show the median across the BEACO<sub>2</sub>N network and the shaded region indicates the 16<sup>th</sup> to 84<sup>th</sup> percentile. Purple shows 6 weeks of data before shelter-in-place (February 2, 2020 through March 14, 2020) and green is 6 weeks during shelter-in-place (March 22, 2020 through May 2, 2020). Blue/yellow background shading is based on cosine of the solar zenith angle with white indicating dawn and dusk.

tially allocated to plausible locations. Errors are assumed to be Gaussian and include off-diagonal terms in both error covariance matrices. Following Rodgers (1990), we solve for the hourly posterior fluxes at 900-m spatial resolution as:

$$\hat{\mathbf{x}} = \mathbf{x}_a + (\mathbf{H}\mathbf{B})^T (\mathbf{H}\mathbf{B}\mathbf{H}^T + \mathbf{R})^{-1} (\mathbf{y} - \mathbf{H}\mathbf{x}_a) \quad (1)$$

where  $\hat{\mathbf{x}}$  ( $m \times 1$ ) is the posterior fluxes,  $\mathbf{x}_a$  ( $m \times 1$ ) is the prior emissions,  $\mathbf{y}$  ( $n \times 1$ ) is the BEACO<sub>2</sub>N observations,  $\mathbf{H}$  ( $n \times m$ ) is the matrix of footprints from HRRR-STILT,  $\mathbf{R}$  ( $n \times n$ ) is the model-data mismatch error covariance matrix, and  $\mathbf{B}$  ( $m \times m$ ) is the prior error covariance matrix (see Supplemental Section S4 for additional details).

Posterior fluxes will reflect the prior fluxes in regions with low sensitivity from the measurements. This can be clearly seen by looking at the gain matrix  $\mathbf{G} = (\mathbf{H}\mathbf{B})^T (\mathbf{H}\mathbf{B}\mathbf{H}^T + \mathbf{R})^{-1}$  and Eq. 1. We can see that  $\hat{\mathbf{x}} \rightarrow \mathbf{x}_a$  in Eq. 1 as  $\mathbf{G} \rightarrow \mathbf{0}$ , indicating that our posterior solution will not deviate from the prior in regions of low sensitivity. As such, we focus our study on regions with high sensitivity because those are the regions that our observations can robustly constrain. Figure 1B shows the region of influence for the BEACO<sub>2</sub>N network. We find the network to be most sensitive to the eastern portion of the San Francisco Bay Area with upwind influence extending east across the bay to San Francisco. The white contour in Figure 1B encapsulates the top 40% of the total of the network sensitivity, hereafter referred to as the “BEACO<sub>2</sub>N Domain”, where we expect strong constraints from the measurements.

### 3 High Resolution Posterior Fluxes

The resulting posterior fluxes inferred using BEACO<sub>2</sub>N observations are shown in Figure 3. Figs. 3A and 3B show the spatial patterns before and during the shelter-in-place order, respectively, while Fig. 3C shows the difference. Changes on roadways are evident in the pattern of differences. Changes to other sectors are more subtle. We have high confidence in the fluxes within the BEACO<sub>2</sub>N Domain because this is the region the BEACO<sub>2</sub>N network is strongly sensitive to, fluxes outside of this region will revert to the prior emissions. Two spatial features that immediately stand out in Fig. 3C are: a 0.4 tC km<sup>-2</sup> hr<sup>-1</sup> decrease in emissions over urban areas within the BEACO<sub>2</sub>N Domain and a modest decrease (0.15 tC km<sup>-2</sup> hr<sup>-1</sup>) across most of the San Francisco Bay

117 Area. We are able to attribute these observed changes to particular sectors because of  
 118 the: 1) high spatial resolution obtained here, 2) satellite observations to constrain the  
 119 biosphere, and 3) detailed prior information available in the region. We find that the mod-  
 120 est regional decrease is due to the biosphere and the large changes in urban areas are  
 121 predominantly due to decreases in traffic.

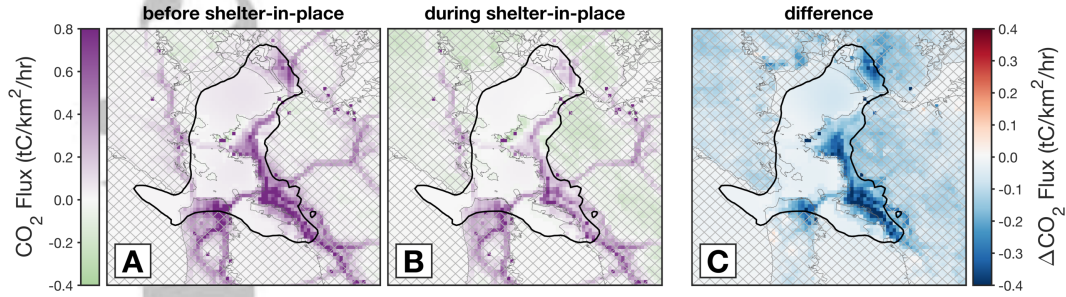


**Figure 3. Spatial patterns of CO<sub>2</sub> fluxes in the San Francisco Bay Area.** Panel A shows the average CO<sub>2</sub> fluxes for 6-weeks before shelter-in-place (February 2, 2020 through March 14, 2020). Panel B shows the average over 6-weeks during shelter-in-place (March 22, 2020 through May 2, 2020). Panel C is the difference. Black contour in all panels is the 60<sup>th</sup> percentile of total network influence (BEACO<sub>2</sub>N Domain). Cross hatching indicates regions with low sensitivity to the BEACO<sub>2</sub>N nodes.

122 Estimating CO<sub>2</sub> fluxes from observations during spring is complicated by the on-  
 123 set of photosynthesis which results in a decrease in atmospheric concentrations. In North-  
 124 ern California, this begins with the grasslands and chaparral in land surrounding the ur-  
 125 ban core. As mentioned above, we use high-resolution satellite observations of SIF from  
 126 TROPOMI to constrain the biospheric activity during this time of year (Turner et al.,  
 127 2020, *under review*), which have been shown to correlate strongly with photosynthetic  
 128 activity (e.g., Frankenberg et al., 2011; Yang et al., 2015, and others). These space-borne  
 129 SIF measurements indicate a 170% (37 tC/hr) increase in daytime CO<sub>2</sub> uptake from the  
 130 biosphere across the BEACO<sub>2</sub>N Domain when comparing before and during the SIP or-  
 131 der. This increase in biospheric activity inferred from space-borne SIF measurements drives  
 132 the regional decrease in CO<sub>2</sub> fluxes shown in Figure 3C.

133 The large changes within the BEACO<sub>2</sub>N Domain coincide with major freeways in  
 134 the San Francisco Bay Area. In particular, the largest decreases are observed over Inter-  
 135 state 880 (I-880) that runs north-south from San Jose to Oakland. Our observational  
 136 network is only sensitive to the northern half of I-880, but the entirety of that section  
 137 shows decreases in CO<sub>2</sub> fluxes in excess of 0.4 tC km<sup>-2</sup> hr<sup>-1</sup>. I-880 is a crucial freeway  
 138 for workers commuting to San Francisco. Other freeways that serve commuters also show  
 139 large decreases in CO<sub>2</sub> fluxes (e.g., Interstates 80 and 580).

140 Figure 4 shows the posterior CO<sub>2</sub> emissions within the BEACO<sub>2</sub>N Domain before  
 141 and during the SIP order. In toto, we observe a 39% decrease in CO<sub>2</sub> fluxes between the  
 142 two time periods. However, the most striking feature is the large perturbation to both  
 143 the daily and weekly cycle of CO<sub>2</sub> fluxes. We observe large CO<sub>2</sub> fluxes that are coinci-  
 144 dent with rush hour before the SIP order. These features are largely absent during the  
 145 SIP order. The pronounced changes in the daily cycle found here highlight the impor-  
 146 tance of incorporating measurements over the course of the day, rather than just the well-  
 147 mixed afternoon as is often done.

148 A common method of characterizing errors in flux inversions is to examine the pos-  
 149 terior error covariance matrix:  $\mathbf{Q} = (\mathbf{H}^T \mathbf{R}^{-1} \mathbf{H} + \mathbf{B}^{-1})^{-1}$ . However,  $\mathbf{Q}$  would have in

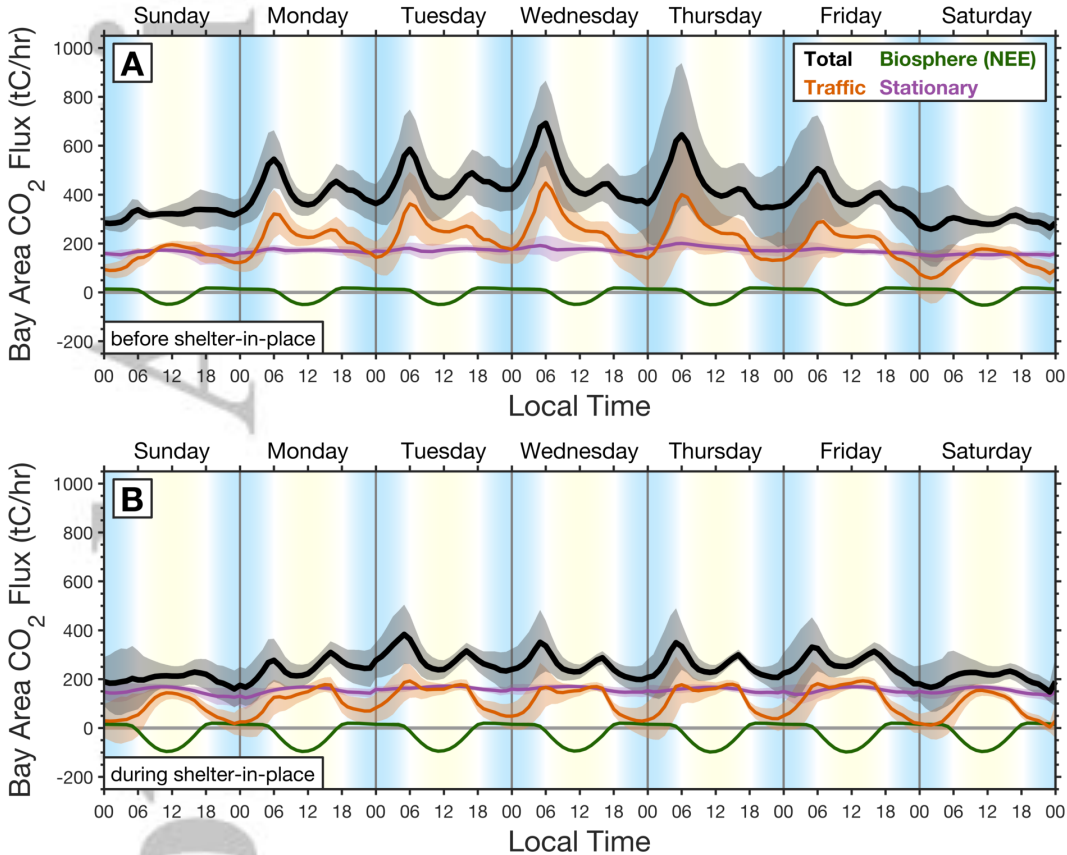


**Figure 4. Weekly cycle of CO<sub>2</sub> fluxes before and during shelter-in-place order.** Solid lines are the weekly mean CO<sub>2</sub> fluxes over the BEACO<sub>2</sub>N Domain (40<sup>th</sup> percentile shown in Fig. 1) and shading is 1- $\sigma$ . Black are the total fluxes. Orange are the traffic emissions. Purple are stationary anthropogenic sources such as: industrial point sources, residential heating, and other non-vehicle anthropogenic sources. Green are the biosphere fluxes (Net Ecosystem Exchange; NEE). Panel A shows emissions before shelter-in-place (February 2, 2020 through March 14, 2020) and panel B shows emissions during shelter-in-place (March 22, 2020 through May 2, 2020).

150 excess of  $10^{13}$  elements here and, assuming single precision, require more than 180 Tb  
 151 to store. As such,  $\mathbf{Q}$  is computationally intractable. We, instead, adopt two methods of  
 152 characterizing the uncertainty: 1) examination of the day-to-day variation and 2)  $k$ -fold  
 153 cross validation. The shaded regions in Fig 4 show the  $1-\sigma$  spread in CO<sub>2</sub> fluxes for given  
 154 hour of the week (i.e., the variation across the 6 weeks). The cross validation is shown  
 155 in Supplemental Section S7 where we find the posterior fluxes to explain 23% more vari-  
 156 ability than the prior fluxes when compared against observations withheld from the flux  
 157 inversion. There is ongoing work comparing these results against independent data of  
 158 traffic flow from the California Department of Transportation (Caltrans, 2020).

159 In our work we solve for total CO<sub>2</sub> fluxes. However, we leverage the high spatial  
 160 resolution obtained here to partition our posterior CO<sub>2</sub> fluxes to specific sectors because  
 161 sources spatially separate as the resolution increases. For example, McDonald et al. (2014)  
 162 demonstrated that 1-kilometer spatial resolution was necessary to distinguish freeways  
 163 from arterial roads. Here, we classify grid cells that have the majority of prior emissions  
 164 coming from a single sector (e.g., we classify a grid cell as “traffic” if more than 50% of  
 165 the prior emissions come from the traffic sector). See Supplemental Section S5 for more  
 166 details.

167 Figure 4 attributes the posterior CO<sub>2</sub> emissions within the BEACO<sub>2</sub>N Domain to  
 168 three sectors, 1) vehicle traffic, 2) stationary anthropogenic emissions, and 3) biogenic.  
 169 Over 80% of the emissions from the stationary sector are due to the industrial point sources  
 170 which likely have small variations over the diurnal cycle. We observe the highest CO<sub>2</sub>  
 171 emissions during the morning rush hour in the middle of the week. This peak is only present  
 172 during the weekdays. Daily average emissions increase from Sunday to their maximum  
 173 on Wednesday and then decrease from Wednesday to Saturday. In contrast, daily av-  
 174 erage emissions during SIP have more subtle differences between weekdays and week-  
 175 ends, as suggested by the day of week variation in the concentrations of CO<sub>2</sub> shown in  
 176 Figure 2. Weekday emissions start earlier than on weekends before and after the SIP or-  
 177 der. After the SIP, rush hour emissions are lower but they still extend emissions earlier  
 178 and later than seen on weekends, resulting in a flatter weekday daytime emissions pro-  
 179 file than on weekends.

180 We find that grid cells classified as stationary sources decreased by 8% (-14 tC/hr)  
 181 in response to the SIP order. The posterior emissions indicate a small diurnal cycle in  
 182 the stationary sector that is largely absent before the SIP order and is not present in the  
 183 prior emissions. In contrast, we find a -48% change (-97 tC/hr) in the weekly average  
 184 CO<sub>2</sub> emissions from grid cells that are classified as freeway whereas emissions. Emissions  
 185 from vehicles at night pre-SIP averaged ~154 tC/hr and during SIP the nighttime emis-  
 186 sions averaged ~55 tC/hr. This represents a 64% decrease in nighttime emissions and  
 187 a 40% decrease during daytime (240 to 144 tC/hr). Independent data from the Califor-  
 188 nia Department of Transportation also indicates a 41% and 34% decrease in vehicle miles  
 189 traveled by cars and trucks, respectively, for road segments in the BEACO<sub>2</sub>N Domain (Caltrans,  
 190 2020).

191 On weekdays before the SIP order, vehicles are the largest source of CO<sub>2</sub> during  
 192 daytime, while on pre-SIP weekends stationary and traffic sources have a comparable mag-  
 193 nitude. After the SIP order, stationary sources are generally the largest term. Such sec-  
 194 toral changes are possible to observe here due to the densely spaced nodes in the BEACO<sub>2</sub>N  
 195 network, allowing us to obtain sub-kilometer spatial resolution and resolve different sec-  
 196 tors.

## 197 4 Conclusions

198 This unnatural experiment conducted in response to COVID-19 has demonstrated  
 199 the subset of CO<sub>2</sub> emissions that are elastic and those that are more entrenched. Emis-

200 sions from traffic are highly elastic and could be rapidly mitigated in response to either  
 201 technological advances or regulations. In contrast, the stationary emissions (e.g., indus-  
 202 trial point sources and residential heating) showed minimal changes in response to the  
 203 shelter-in-place order. This implies that those sources are more entrenched and will re-  
 204 quire longer-time scales to mitigate if we hope to limit future warming. These findings  
 205 provide a glimpse into a future where CO<sub>2</sub> emissions from vehicle traffic are reduced through  
 206 the electrification of the vehicle fleet, which would also have air quality co-benefits; ob-  
 207 serving these CO<sub>2</sub> emission changes from such a transition will require sustained mea-  
 208 surements as the changes will be more subtle than the abrupt 48% changes seen here.

## 209 Acknowledgments

210 We thank B. Fasoli for recent developments to the STILT model and sharing pre-processing  
 211 code, E. Delaria for developing a temperature calibration, P. Vannucci and A. Lall for  
 212 feedback, and former members of the BEACO<sub>2</sub>N project for establishing the network:  
 213 A. A. Shusterman, V. Teige, and K. Lieschke. The author acknowledges ideas and ad-  
 214 vice from the participants in the COVID-19 and Earth System Science workshop orga-  
 215 nized by the W.M. Keck Institute for Space Studies. We are grateful to the team that  
 216 has realized the TROPOMI instrument, consisting of the partnership between Airbus  
 217 Defence and Space, KNMI, SRON, and TNO, commissioned by NSO and ESA. **Fund-**  
 218 **ing:** AJT was supported as a Miller Fellow with the Miller Institute for Basic Research  
 219 in Science at UC Berkeley. This research was funded by grants from the Koret Founda-  
 220 tion and University of California, Berkeley. Part of this research was funded by the NASA  
 221 Carbon Cycle Science program (grant NNX17AE14G). TROPOMI SIF data generation  
 222 by PK and CF is funded by the Earth Science U.S. Participating Investigator program  
 223 (grant NNX15AH95G). This research used the Savio computational cluster resource pro-  
 224 vided by the Berkeley Research Computing program at the University of California, Berke-  
 225 ley (supported by the UC Berkeley Chancellor, Vice Chancellor for Research, and Chief  
 226 Information Officer). **Author contributions:** AJT and RCC wrote the text with feed-  
 227 back from all authors. JK, HF, CN, KW, KC, and PJW collected CO<sub>2</sub> data. PK and  
 228 CF performed the TROPOMI SIF retrieval. AJT conducted the numerical modeling,  
 229 analysis, downscaled SIF data, and drafted figures. **Competing interests:** The authors  
 230 declare no competing interests. **Data and materials availability:** CO<sub>2</sub> is available  
 231 at <http://beacon.berkeley.edu/>. Code has been deposited in GitHub,  
 232 <https://www.github.com/alexjturner/UrbanInversion>.

## 233 References

- 234 Caltrans. (2020). *Performance Measurement System Data Source*. California Depart-  
 235 ment of Transportation. Retrieved from <http://pems.dot.ca.gov>
- 236 Contra Costa County Health Officer. (2020). *Contra Costa County Shelter-in-  
 237 Place Order*. Contra Costa County. Retrieved from <https://cchealth.org/coronavirus/pdf/H0-COVID19-SIP-0316-2020.pdf>
- 238 EIA. (2015). *Emissions of Greenhouse Gases in the U.S.* (Tech. Rep.). U.S. Energy  
 239 Information Administration.
- 240 Fasoli, B., Lin, J. C., Bowling, D. R., Mitchell, L., & Mendoza, D. (2018). Sim-  
 241 ulating atmospheric tracer concentrations for spatially distributed receptors:  
 242 updates to the Stochastic Time-Inverted Lagrangian Transport model's R  
 243 interface (STILT-R version 2). *Geoscientific Model Development*, 11(7), 2813-  
 244 2824. doi: 10.5194/gmd-11-2813-2018
- 245 Frankenberg, C., Fisher, J. B., Worden, J., Badgley, G., Saatchi, S. S., Lee, J.-E.,  
 246 ... Yokota, T. (2011). New global observations of the terrestrial carbon cycle  
 247 from GOSAT: Patterns of plant fluorescence with gross primary productivity.  
 248 *Geophys Res Lett*, 38(17). doi: 10.1029/2011gl048738
- 249 Hutyra, L. R., Duren, R., Gurney, K. R., Grimm, N., Kort, E. A., Larson, E., &

- 251 Shrestha, G. (2014). Urbanization and the carbon cycle: Current capabilities  
 252 and research outlook from the natural sciences perspective. *Earth's Future*,  
 253 2(10), 473-495. doi: 10.1002/2014ef000255
- 254 IPCC. (2013). *Climate Change 2013: The Physical Science Basis. Contribution*  
 255 *of Working Group I to the Fifth Assessment Report of the Intergovernmental*  
 256 *Panel on Climate Change* (Tech. Rep.). Author.
- 257 IPCC. (2018). *Global Warming of 1.5°C. An IPCC Special Report on the im-*  
 258 *pacts of global warming of 1.5°C above pre-industrial levels and related global*  
 259 *greenhouse gas emission pathways, in the context of strengthening the global*  
 260 *response to the threat of climate change, sustainable development, and efforts*  
 261 *to eradicate poverty* (Tech. Rep.). Author.
- 262 Kenyon, J. S., Moninger, W. R., Smith, T. L., Peckham, S. E., Lin, H., Grell, G. A.,  
 263 ... Manikin, G. S. (2016). A North American Hourly Assimilation and Model  
 264 Forecast Cycle: The Rapid Refresh. *Monthly Weather Review*, 144(4), 1669-  
 265 1694. doi: 10.1175/mwr-d-15-0242.1
- 266 Kim, J., Shusterman, A. A., Lieschke, K. J., Newman, C., & Cohen, R. C. (2018).  
 267 The BErkeley Atmospheric CO<sub>2</sub> Observation Network: field calibration and  
 268 evaluation of low-cost air quality sensors. *Atmospheric Measurement Tech-*  
 269 *niques*, 11(4), 1937-1946. doi: 10.5194/amt-11-1937-2018
- 270 Le Quéré, C., Jackson, R. B., Jones, M. W., Smith, A. J. P., Abernethy, S., Andrew,  
 271 R. M., ... Peters, G. P. (2020). Temporary reduction in daily global CO<sub>2</sub>  
 272 emissions during the COVID-19 forced confinement. *Nature Climate Change*.  
 273 doi: 10.1038/s41558-020-0797-x
- 274 Lin, J. C., Gerbig, C., Wofsy, S. C., Andrews, A. E., Daube, B. C., Davis, K. J., &  
 275 Grainger, C. A. (2003). A near-field tool for simulating the upstream influ-  
 276 ence of atmospheric observations: The Stochastic Time-Inverted Lagrangian  
 277 Transport (STILT) model. *J Geophys Res-Atmos*, 108(D16), 4493-4510. doi:  
 278 Artn4493D0i10.1029/2002jd003161
- 279 McDonald, B. C., McBride, Z. C., Martin, E. W., & Harley, R. A. (2014). High-  
 280 resolution mapping of motor vehicle carbon dioxide emissions. *J Geophys Res-*  
 281 *Atmos*, 119(9), 5283-5298. doi: Doi10.1002/2013jd021219
- 282 Rodgers, C. D. (1990). Characterization and Error Analysis of Profiles Retrieved  
 283 from Remote Sounding Measurements. *J Geophys Res-Atmos*, 95(D5), 5587-  
 284 5595. doi: Doi10.1029/Jd095id05p05587
- 285 Shusterman, A. A., Kim, J., Lieschke, K. J., Newman, C., Wooldridge, P. J., &  
 286 Cohen, R. C. (2018). Observing local CO<sub>2</sub> sources using low-cost, near-  
 287 surface urban monitors. *Atmos Chem Phys*, 18(18), 13773-13785. doi:  
 288 10.5194/acp-18-13773-2018
- 289 Shusterman, A. A., Teige, V. E., Turner, A. J., Newman, C., Kim, J., & Co-  
 290 hen, R. C. (2016). The BErkeley Atmospheric CO<sub>2</sub> Observation Net-  
 291 work: initial evaluation. *Atmos Chem Phys*, 16(21), 13449-13463. doi:  
 292 10.5194/acp-16-13449-2016
- 293 Turner, A. J., Jacob, D. J., Benmergui, J., Brandman, J., White, L., & Randles,  
 294 C. A. (2018). Assessing the capability of different satellite observing config-  
 295 urations to resolve the distribution of methane emissions at kilometer scales.  
 296 *Atmos Chem Phys*, 18(11), 8265-8278. doi: 10.5194/acp-18-8265-2018
- 297 Turner, A. J., Köhler, P., Magney, T. S., Frankenberg, C., Fung, I., & Cohen,  
 298 R. C. (2020). A double peak in the seasonality of California's photo-  
 299 synthesis as observed from space. *Biogeosciences*, 17(2), 405-422. doi:  
 300 10.5194/bg-17-405-2020
- 301 Turner, A. J., Köhler, P., Magney, T. S., Frankenberg, C., Fung, I., & Cohen, R. C.  
 302 (*under review*). Extreme events driving year-to-year differences in gross pri-  
 303 mary productivity across the US. *Geophysical Research Letters*, XX(XX),  
 304 XX-XX. doi: 10.1002/2020glXXXXXX
- 305 Turner, A. J., Shusterman, A. A., McDonald, B. C., Teige, V., Harley, R. A., &

- 306 Cohen, R. C. (2016). Network design for quantifying urban CO<sub>2</sub> emissions:  
307 assessing trade-offs between precision and network density. *Atmos Chem Phys*,  
308 16(21), 13465-13475. doi: 10.5194/acp-16-13465-2016
- 309 Yang, X., Tang, J., Mustard, J. F., Lee, J.-E., Rossini, M., Joiner, J., ... Richard-  
310 son, A. D. (2015). Solar-induced chlorophyll fluorescence that correlates  
311 with canopy photosynthesis on diurnal and seasonal scales in a temper-  
312 ate deciduous forest. *Geophysical Research Letters*, 42(8), 2977-2987. doi:  
313 10.1002/2015gl063201

Accepted Article